*Environ. Sci. Technol.* **2008,** *42,* 2949–2956

# X-ray Microtomography Determination of Air–Water Interfacial Area–Water Saturation Relationships in Sandy Porous Media

MOLLY S. COSTANZA-ROBINSON,* KATHERINE H. HARROLD,† AND ROSS M. LIEB-LAPPEN

*Environmental Studies Program and Department of Chemistry and Biochemistry, Middlebury College, McCardell Bicentennial Hall 446, Middlebury, Vermont 05753*

*Received August 20, 2007. Revised manuscript received January 2, 2008. Accepted January 22, 2008.*

In this work, total smooth air–water interfacial areas were measured for a series of nine natural and model sandy porous media as a function of water saturation using synchrotron X-ray microtomography. Interfacial areas decreased linearly with water saturation, while the estimated maximum interfacial area compared favorably to the media geometric surface areas. Importantly, relative interfacial area (i.e., normalized by geometric surface area) versus water saturation plots for all media collapsed into a single linear cluster ($r^2 = 0.93$), suggesting that geometric surface area is an important, and perhaps sufficient, descriptor of sandy media that governs total smooth interfacial area–water saturation relationships. Measured relationships were used to develop an empirical model for estimating interfacial area–water saturation relationships for sandy porous media. Model-based interfacial area estimates for independent media were generally slightly higher than interfacial areas measured using aqueous-phase interfacial tracer methods, which may indicate that microtomography captures regions of the air–water interface that are not accessible to aqueous-phase interfacial tracers. The empirical model presented here requires only average particle diameter and porosity as input parameters and can be used to readily estimate air–water interfacial area–water saturation relationships for sandy porous media.

## Introduction

The air–water interface in variably saturated porous media significantly influences the retention of organic compounds and colloids (*1–8*), wetting/drying hysteresis (*9–11*), and mass-transfer processes, such as aqueous dissolution, volatilization, and evaporation (*12*). Despite such importance, explicit accounting for interfacial processes (e.g., in solute transport models) has been hampered by uncertainty in measured air–water interfacial areas. Several techniques have been proposed to measure air–water interfacial areas in porous media and two-dimensional media analogs, including aqueous and gas-phase interfacial tracer techniques (*5, 9–11, 13–17*). With regard to the most basic trends in interfacial parameters, interfacial tracer methods are in agreement; for example, all methods reveal that interfacial areas are inversely related to water saturation and proportional to the surface area of the medium. Despite these commonalities, measured interfacial areas, even for similar porous media, can vary by several orders of magnitude depending on which measurement method is used (*16, 18–21*). It is hypothesized that the considerable variation in measured interfacial areas may derive from the fact that different methods actually capture different contributions to the total interfacial area (i.e., capillary, thin-film, and interfacial micromorphology). Because of the indirect nature of interfacial tracer measurement methods, it has remained difficult to assess which interfacial domains are captured by various methods.

Recently, synchrotron X-ray microtomography ($\mu$CT) has shown promise for direct investigation of the air–water interface in variably saturated porous media (*22*). The direct nature of the image-based measurement provides explicit knowledge of which interfacial domains are represented by the measured interfacial areas. Specifically, $\mu$CT has been shown to capture both the capillary and thin-film interfacial domains, but explicitly excludes interfacial micromorphology (*20, 21, 23*); thus, $\mu$CT image-derived interfacial areas represent total "smooth" air–water interfaces. Development of $\mu$CT methods for air–water interfacial area determination is in its early stages, however, and has only been applied to a handful of porous media systems (*20, 21, 23*). Limits of the application have not been sufficiently defined, nor have image processing methods been validated for a variety of porous media.

In this work, $\mu$CT was used to measure air–water interfacial area–water saturation relationships for a series of nine model and natural sandy porous media. Two objectives guided the work: (1) to evaluate the applicability and limitations of $\mu$CT methods for total smooth air–water interfacial area determination in a variety of sandy porous media; and (2) to develop an empirical $\mu$CT-based model of total smooth interfacial area–water saturation relationships for sandy porous media. The utility of the empirical model was assessed by estimation of interfacial area–water saturation relationships for a variety of porous media systems for which independent measurements were available.

## Experimental Section

**Porous Media Properties and Sample Preparation.** Sand-sized glass beads (GB) (MO-SCI Specialty Products) and two commercial silica sands, Granusil and Accusand (Unimin Corporation), were studied. Media were sieved to achieve well-sorted fractions of varying texture; fractions were also combined to create poorly sorted mixtures. Media were chosen to represent a range of particle shape and surface roughness, as represented by the ratio of surface areas measured by gas adsorption (e.g., $N_2$/BET) to geometric surface areas (i.e., calculated under a smooth-sphere assumption). Relevant properties of the porous media studied are provided in Table 1 (SEM images of media are provided in Figure S1 of the Supporting Information).

Porous media were packed in custom-made, X-ray transparent, anodized aluminum microcolumns (4.7 mm i.d. × 40 mm) fitted with PEEK-encased 316 stainless steel dispersion frits (2 $\mu$m, Isolation Technologies) and sealed with aluminum compression fittings or threaded PTFE caps. The influence of two wetting methods on measured interfacial areas was evaluated: (a) premixing of the porous media with water to achieve the desired water saturation followed by wet-packing and (b) dry-packing

* Corresponding author phone: (802) 443-5571; fax: (802) 443-2072; e-mail: mcostanz@middlebury.edu.

† Now at San Francisco Estuary Institute, Oakland, California 94621.

10.1021/es072080d CCC: $40.75 
Published on Web 03/15/2008

**TABLE 1. Physical Properties of Porous Media**

| porous medium | $d_{50}$ ($\mu$m) | $U^c$ | volume-normalized surface area ($cm^{-1}$) $N_2$–BET[a] | geometric, SA[b] | SRF[d] |
|---|---|---|---|---|---|
| | | | glass bead | | |
| fine | 99 | 1.1 | 780 | 365 | 2 |
| medium | 345 | 1.2 | 211 | 113 | 2 |
| coarse | 650 | 1.1 | 296 | 55 | 5 |
| mix | 403 | 4.6 | 545 | 97 | 6 |
| | | | Accusand | | |
| medium | 375 | 1.2 | 1776 | 101 | 18 |
| coarse | 516 | 1.2 | 2103 | 73 | 29 |
| | | | Granusil | | |
| fine | 200 | 1.7 | 8173 | 162 | 50 |
| coarse | 513 | 1.7 | 5648 | 65 | 87 |
| mix | 211 | 2.9 | 5175 | 163 | 32 |

[a] Micrometrics, Inc. (Norcross, GA). [b] Geometric surface area, SA = $6(1-n)/d_{50}$. [c] Uniformity coefficient, $U = d_{60}/d_{10}$. [d] Shape/roughness factor, SRF = $S_a$/SA.

followed by water imbibition to near-saturation and subsequent flushing with air. For both wetting methods, iodide-doped water (13 or 20% KI by mass) was used to enhance $\mu$CT image contrast (*22*). Wet-packed columns were imaged at a single water saturation. For imbibed columns, the KI solution (referred to hereafter as "water") was pumped into the inlet until saturation was achieved; the column was then iteratively imaged and drained by flushing with air. A single imbibed-column packing was imaged at up to four water saturations.

**Synchrotron Microtomography and Image Processing.** Synchrotron X-ray microtomography ($\mu$CT) was performed on the GeoSoilEnviro Consortium for Advanced Radiation Sources (GSECARS) Beamline 13-BM-D at the Advanced Photon Source at Argonne National Laboratory. Image collection methods were similar to those described elsewhere (*20–24*). Briefly, images were obtained at 10.6–11.3 $\mu$m resolution 100 eV above and below the X-ray absorption edge of iodide (33.169 keV). Generally, a single vertical section of the column (~5.5 mm) was imaged; some columns were imaged at multiple locations. Raw scan data underwent reconstruction and preprocessing using algorithms developed at GSECARS (*25*). Quantitative analysis was performed on a central cuboid (~80 $mm^3$) of the full three-dimensional image volume. Blob3D (*26*) software was used to median smooth ($1 \times 1 \times 1$) the image grayscale intensities.

A multistep process, depicted in Figure 1, was developed to assign image voxels to either the solid, air, or water phases based on the grayscale intensity of the voxel. This segmentation process relied on information integrated across multiple images of the same sample. The air phase was segmented from images collected at X-ray energies below the iodide absorption edge (i.e., below-edge images). For below-edge images, the threshold grayscale intensity for segmentation was taken as the minimum in the grayscale intensity histogram for the median-smoothed image and adjusted slightly based on visual correspondence between the air phases in the original and segmented below-edge images (see Figure S2 for representative grayscale histograms and comparison of original and segmented below-edge images).

The water phase was segmented from a "difference image" that was created by subtracting the below-edge images from the corresponding above-edge images; the difference image provides direct visualization of the iodide-doped water phase. Grayscale intensity histograms for difference images did not contain a distinct minimum; therefore, segmentation of the water phase was based on visual correspondence between the original and segmented difference images (see Figure S3 for representative grayscale histograms and comparison of original and segmented difference images).

Finally, segmented below-edge (air) and difference images (water) were merged by masking the air phase over the water phase and allowing the porous media to be defined implicitly (IDL (ITT Visual Information Systems)). This masking approach conserves the original air segmentation and reflects the higher confidence in the air segmentation due to the distinct grayscale intensity histogram minimum present in the below-edge images. The product of this multistep image manipulation is a "trinary" image, in which the three bulk phases (air, water, solid) are each represented by a unique grayscale value (Figure 1).

Quantitative information for the water phase could be obtained solely from the difference images and separately for the air phase from the below-edge images. The benefit of creating and extracting quantitative data from the merged trinary image is that the trinary image is fully segmented, meaning that every voxel is assigned to one of the three bulk phases (i.e., no voxels are left unassigned) and that no voxel is "double-assigned" to more than one phase. Such inconsistencies were observed when data were extracted from multiple images independently of each other.

Phase volumes and surface areas were extracted from trinary images using Blob3D (*26*). Surface areas were subjected to a $3 \times 3 \times 3$ smoothing filter to minimize surface area enhancement due to image voxelation. The volume-normalized smoothed surface area of the air phase was taken as the total smooth air–water interfacial area, based on the assumption that the quartz sands and glass bead media were water-wetted (*20, 21*). Average porosity and water saturation were determined from the air- and water-phase volumes in the trinary image. The total smooth air–water interface in the trinary image was visualized using Amira software and constrained smoothing ($3 \times 3 \times 3$) triangulation methods.

## Results and Discussion

**Validation of Image Processing Methods.** The quality of quantitative information derived from $\mu$CT images relies directly on the accuracy in assigning image voxels to the air, water, or solid phases (i.e., segmentation quality). Qualitatively, the accuracy of the segmentation can be assessed by comparison of the original above-edge and the trinary images, as shown in Figure 2. The comparison is quite favorable for all but the GB fine medium. The segmentation of the GB fine medium was less accurate and, indeed, difficult to even qualitatively assess due to the small particle and pore sizes. In fact, the surface smoothing algorithm used to minimize voxelation artifacts could not be successfully applied to the GB fine medium, due to difficulties in smoothing objects consisting of so few voxels. The average diameter of GB fine particles (~100 $\mu$m) represents ~10 pixels; thus, caution should be used in interpreting extracted quantitative data obtained for similarly low particle-to-pixel size ratios. For our purposes, GB fine was excluded from further quantitative analysis. Interestingly, the GB mix medium contains 15% (wt) GB fine, but due to the preferential capillary filling of the smaller pores associated with regions of the media containing small particles, very little of the air–water interface is associated with the finer particles. Thus, except for the GB fine system, segmentation was qualitatively considered as successful for the systems examined here.

A quantitative measure of segmentation quality is potentially obtained by comparison of image-derived and independent measures of water content and porosity; however, dead volume in the microcolumn was comparable to the pore volume of the media (~0.3 $cm^3$), resulting in significant uncertainty in gravimetric measures. Thus, segmentation quality was quantitatively evaluated via examination of the image-derived information for the solid phase.

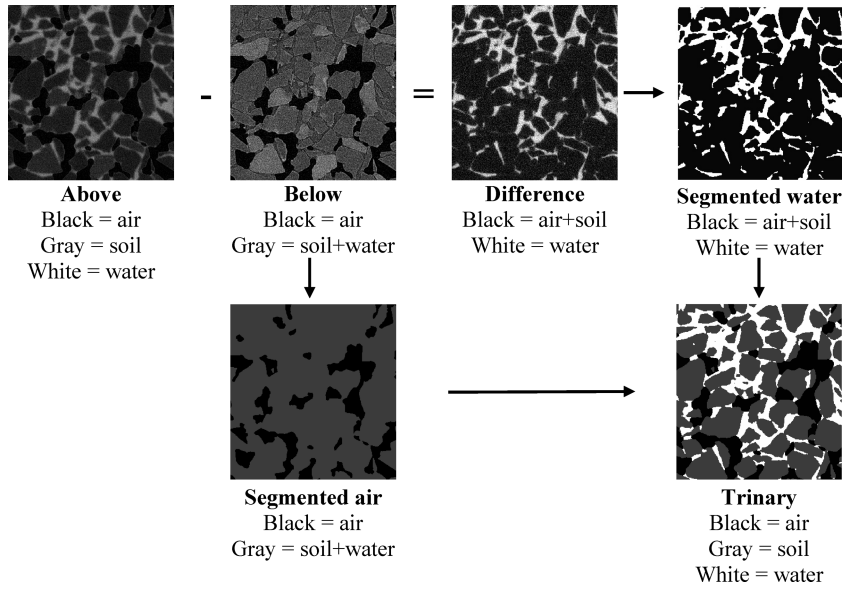


**FIGURE 1. Schematic depicting the creation of a segmented trinary image from which interfacial areas were extracted, shown here for Granusil coarse (46% $S_w$).**

Because the solid phase was defined only implicitly when creating the trinary image, its quantitative features are governed by the segmentation accuracy of both the below-edge and difference images. As such, validation of the solid-phase data provides a measure of segmentation quality that integrates over the entire image processing, segmentation, and data extraction procedure used. Image-derived solid-phase surface areas agreed closely with geometric surface areas for all media (Figure S4), with greatest variation observed for the Granusil mix (6% rsd) and GB mix (10% rsd). The greater variation in the poorly sorted media is attributed primarily to differences in the particle size distribution between different imaged locations within a given sample and to differences between sample packings rather than to differences in segmentation. Image-derived surface areas were independent of water saturation, indicating that the segmentation procedures were consistently applied across the water saturation range investigated here.

**Visualization of the Total Smooth Air–Water Interface.** Porescale visualizations of the measured total smooth air–water interface for coarse media are shown in Figure 3. Under wet conditions, total interfacial areas were lower, and air blobs were more disconnected and exhibited greater similarity in shape across media. Under dry conditions, the differences in porous media particle shape were readily apparent: the glass beads appear spherical; Accusand appears nonspherical and rounded; and Granusil, despite surface smoothing, retained its angular particle shape (see Figure S1 for SEM images of porous media). Assuming that particle surfaces were water-solvated, these images reveal the important interfacial area contributions of adsorbed water films and of underlying particle shape on macroscopic air–water interfacial morphology. Importantly, however, the surface smoothing algorithm that was used to minimize overestimation of interfacial areas due to imaging artifacts (i.e., voxelation), also masks real interfacial micromorphology that is created by the surface roughness of particles underlying the thin water films. As such, the interfacial areas extracted from such images are considered as total smooth interfacial areas, which explicitly exclude interfacial micromorphology.

**Total Smooth Air–Water Interfacial Areas.** Volume-normalized air–water interfacial areas were extracted from the three-dimensional images and are shown as a function of water saturation in Figure 4. All media types and size fractions display linear inverse interfacial area−water saturation relationships; no influence of porous media wetting method or iodide-dopant concentration is evident. The observed inverse relationship is consistent with the experimental and modeling air–water interface literature (*11, 16, 18–21, 23, 27*). The linearity of the relationship and magnitude of the interfacial areas are also qualitatively consistent with measurements for similar media made using aqueous-phase interfacial tracer methods (*9, 11, 14, 15, 20, 28*) and for a fine aquifer sand measured using $\mu$CT (*20, 21*). A similar linear interfacial area−water saturation relationship has also been reported by studies using computational approaches that considered smoothed thin-film contributions to the air–water interface (*19, 29, 30*). The similarity between $\mu$CT and aqueous-phase interfacial tracer data suggest that aqueous-phase interfacial tracers may be capturing both capillary and thin-film contributions to the air–water interface and, like $\mu$CT, exclude interfacial area contributed by interfacial micromorphology. This stands in contrast to gas-phase interfacial tracer methods, for which nonlinear interfacial area−water saturation relationships are observed and considerably larger interfacial areas are reported, presumably due to inclusion of interfacial micromorphology (*5, 16, 31*).

**Interfacial Area Dependence on Porous Medium Properties.** The linear interfacial area−water saturation relationships (Figure 4) can be extrapolated to 0% $S_w$ to obtain an estimate of the maximum interfacial area for each porous medium, which corresponds to dry systems in which only a thin film of water coats each particle. Thus, maximum interfacial areas and geometric surface areas for each porous medium are expected to be comparable, as was observed (Figure S5). In contrast, no correlation was observed between maximum interfacial areas and surface areas measured by $N_2$/BET adsorption, which captures the influence of particle roughness. For example, Accusand and GB medium, despite ~8-fold difference in $N_2$/BET surface areas (1776 versus 211 $cm^{-1}$), have quite similar maximum interfacial areas (82 and 87 $cm^{-1}$) and quite similar geometric surface areas (Table 1). Likewise, despite similar $N_2$/BET surface areas for Granusil coarse and Granusil mix (5648 and 5175 $cm^{-1}$), the maximum interfacial area and geometric surface area for the Granusil mix are both ~2.5 times greater due to the smaller average particle size in the poorly sorted media. The agreement between maximum interfacial areas and geometric surface areas suggests that for the model and natural porous media investigated here, the image processing methods, including

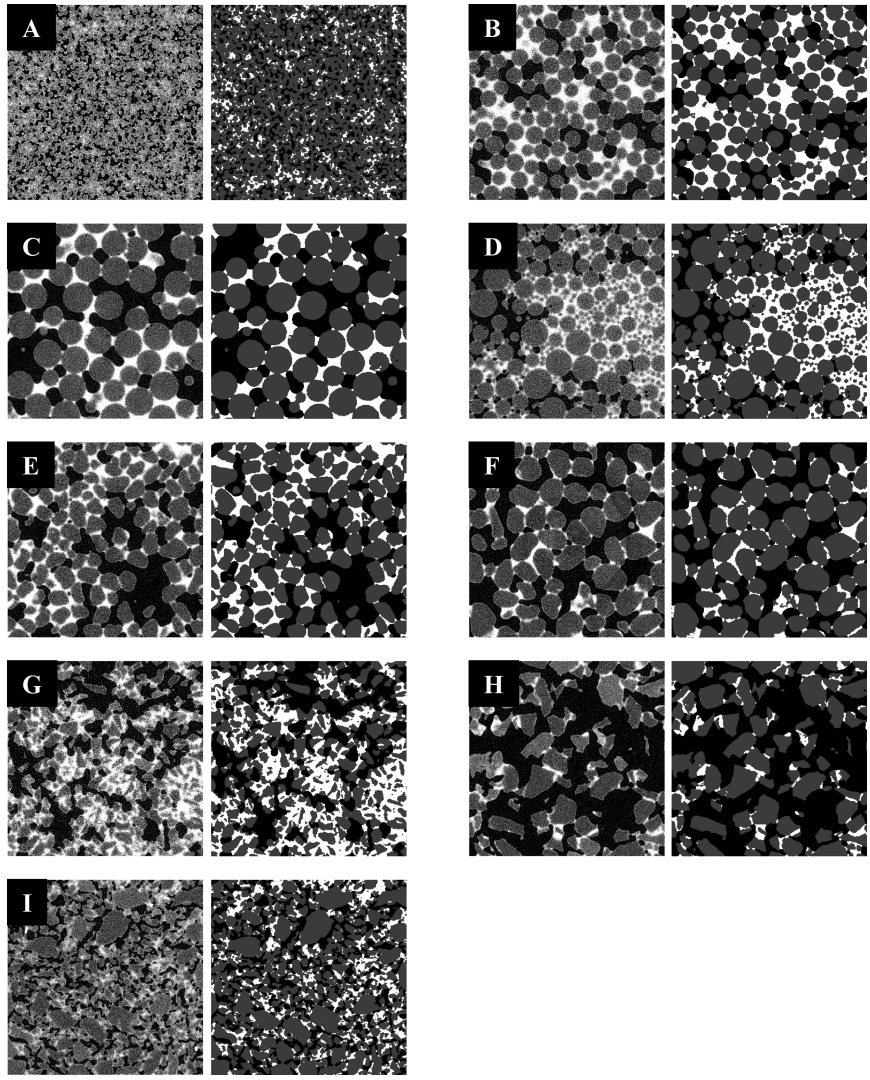


**FIGURE 2. Representative above-edge images (left) and corresponding trinary images (right) shown for Glass Bead fine, medium, coarse, and mix (A–D); Accusand medium and coarse (E and F); and Granusil fine, coarse, and mix (G–I), respectively. Black = air; gray = porous media; white = water.**

surface area smoothing, retain defining characteristics of the media both visually (i.e., the particle shape is evident in processed images) and quantitatively. It also appears that interfacial areas measured by $\mu$CT are governed primarily by average particle size (the key parameter used in estimating geometric surface areas) and that even for the angular natural media investigated here (e.g., Granusil), particles are reasonably represented as spheres.

Normalizing measured interfacial areas by geometric surface areas yields relative interfacial areas and allows the influence of factors other than average particle size on the interfacial area–water saturation relationship to be observed. As shown in Figure 5, relative interfacial area–water saturation relationships for all media and size fractions collapsed into a single linear cluster. The uniform relationship exhibited by all porous media studied was both surprising and important; it suggests that average particle size (i.e., geometric surface area) and water saturation may be sufficient and general predictors of total smooth interfacial areas for sandy media. This stands in contrast to similar measurements made using gas-phase tracers (*27*), for which relative interfacial area–water saturation plots were observed to be nonlinear and exhibited distinctly different behavior for each porous medium. The nonlinearity and porous-media specific nature of measurements made using gas-phase tracers is presumably due to the sensitivity of gas-phase tracer methods to surface roughness (*19, 27*), thereby rendering particle size an insufficient descriptor of interfacial areas measured by gas-phase tracers.

**Empirical Model Development and Evaluation.** The strong linear correlations observed for both maximum interfacial area–geometric surface area and relative interfacial area–water saturation relationships allowed development of an empirical model of total smooth interfacial area–water saturation relationships for sandy porous media that requires only knowledge of geometric surface area. Integration of image-derived linear regressions (Figures S5 and 5) yield

$$A_{ia}(\mathrm{cm}^{-1}) = \mathrm{SA}[(-0.9112)S_w + 0.9031] \qquad (1)$$

where $A_{\mathrm{ia}}$ is the total smooth interfacial area, SA is the geometric surface area calculated as (*32*)

$$\frac{6(1-n)}{d_{50}} \qquad (2)$$

and $S_{\mathrm{w}}$ is water saturation. Using eq 1, the entire interfacial area–water saturation relationship can be readily estimated with few experimental measurements, which are often time-consuming or require elaborate experimental facilities (e.g., synchrotron $\mu$CT). For example, interfacial area could be

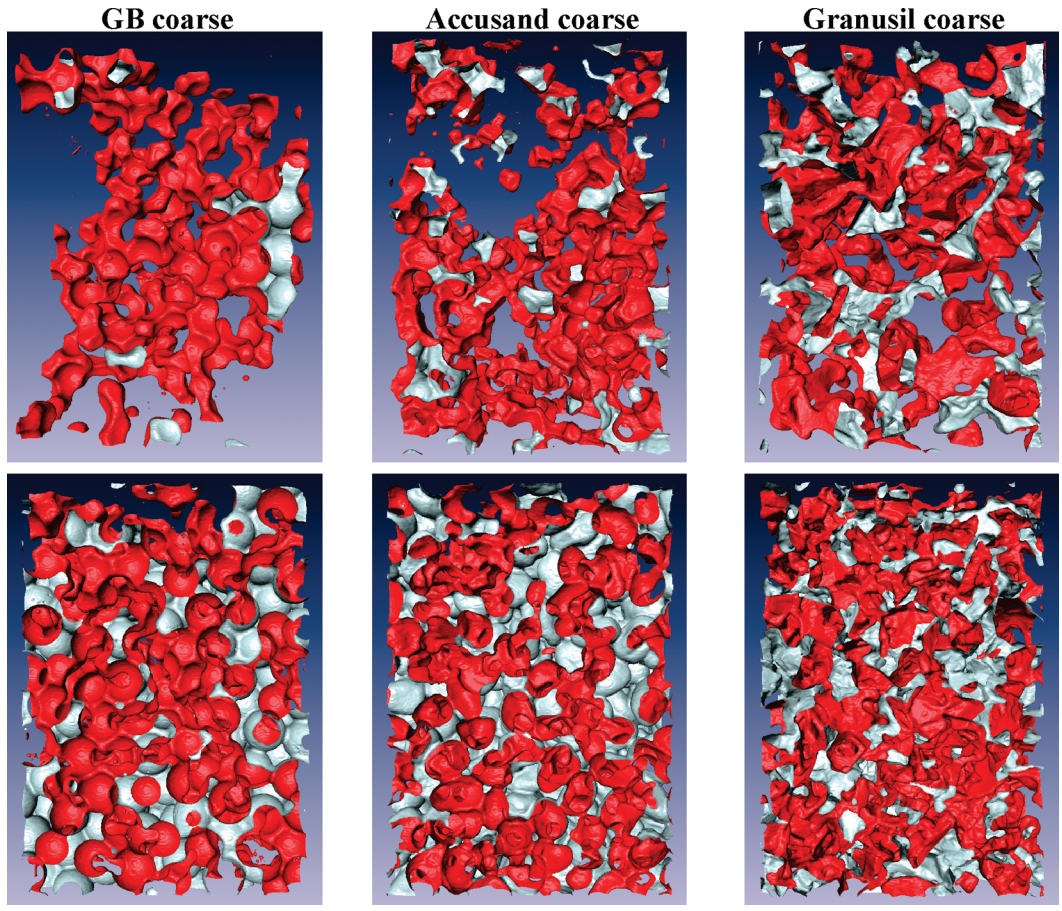


**FIGURE 3. Visualization of the total smooth air–water interface under representative wet (top) and dry (bottom) conditions for coarse media. Red and gray represent the exterior and interior surfaces of the air–water interface, respectively.**

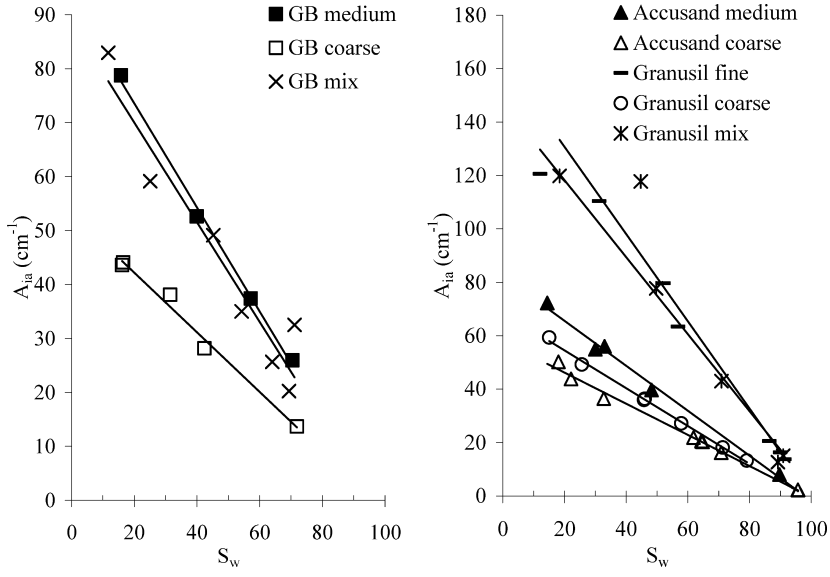


**FIGURE 4. Total smooth interfacial area ($A_{ia}$) as a function of water saturation ($S_w$) ($r^2 \geq 0.91$ for all media).**

measured experimentally at a single water saturation to verify the assumptions of the model are satisfied by the porous medium of interest (e.g., reasonably spherical particle shape), and interfacial areas at remaining water saturations simply estimated using eq 1. Additionally, the ability of $\mu$CT to capture the entirety of the air–water interface without the kinetic or accessibility limitations inherent to tracer-based measurement methods allows this empirical model to be used as a benchmark of the total smooth interfacial areas−water saturation functions against which other indirect measurement methods can be compared.

To evaluate the utility of the empirical model, eq 1 was used to independently predict air–water interfacial area relationships for a variety of model and natural sandy porous media for which experimental data were available (*9, 11, 14, 15, 21, 28, 33*). Because aqueous-phase tracers are thought to measure the same interfacial domains as $\mu$CT (i.e., capillary and film contributions, excluding micromorphology), only interfacial

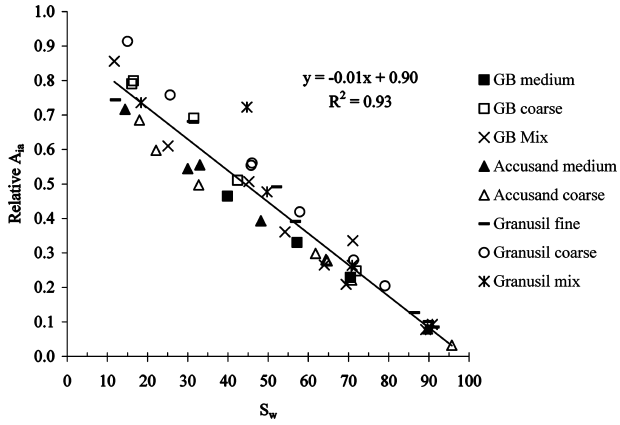


**FIGURE 5. Relative interfacial area (interfacial area normalized by geometric surface area) versus water saturation ($S_w$).**

areas measured using aqueous-phase tracers were compared here. As shown in Figure 6, eq 1 generally results in slightly higher estimated interfacial areas than were experimentally determined, although in a third of the cases (data sets D, F, G, and J), the predictions and experimental determinations are in close agreement. Only in two cases (data sets I and L) do the measured interfacial areas exceed those derived from eq 1. Although relatively few data sets were available to represent each aqueous-phase method, no obvious method-dependence in the degree of agreement between the estimated and experimental values was observed. Moreover, both glass beads and natural sands had similar correspondence between measured and estimated interfacial areas, suggesting that failure of the geometric surface area assumption (e.g., spherical particles) is not an important cause of the discrepancy.

The generally higher interfacial areas derived from the $\mu$CT-based empirical model may indicate that image artifacts (e.g., voxelation) are contributing to an overestimate of image-based interfacial areas despite the surface smoothing methods employed here. Further work is needed to clarify the influence of surface smoothing algorithms in minimizing voxelation artifacts, while simultaneously retaining characteristic porous media properties (e.g., particle shape). Moreover, the KI dopant used to enhance $\mu$CT image contrast may increase water surface tensions, and thereby alter water distributions, although this is not supported by the data here in which KI concentrations of 13 and 20% were not observed to influence measured interfacial areas. Alternatively, the higher $\mu$CT estimates may suggest that $\mu$CT is able to capture regions of the air–water interface that are not accessible to aqueous-phase tracers. For example, interface associated with isolated air pockets may be inaccessible to advective interfacial tracers and also, via rate-limitations, to diffusive tracers. This is consistent with computational results, in which interfacial areas measured by aqueous-phase tracers exceeded modeling results for capillary-only contributions to the air–water interface, but were lower than modeled total smooth interfacial areas (*19*).

Discrepancies between modeled and measured interfacial areas may also be due to uncertainties inherent to aqueous-phase interfacial area estimates, such as rate-limited diffusion of the tracer to the air–water interface, nonlinear sorption isotherms of the surfactant tracers to the solid phase, and by changes in fluid distributions due to decreased surface tension caused by the interfacial tracers (surfactants) used. Investigations of the influence of lower surface tensions on measured interfacial areas, however, reveal little influence (*9*) or a slight increase in measured interfacial areas (*11*), which would not explain the difference reported here between the experimental data and empirical model estimates.

**Implications.** The synchrotron $\mu$CT and image processing methods developed here allowed quantitative porescale investigation of the air–water interface in variable saturated porous media and were shown to be applicable to a variety of water-wet model and natural sandy porous media. Limitations were observed, however, for the segmentation of images for fine-grained porous media with particle-to-pixel size ratio of ~10. The lowest successful particle-to-pixel ratio investigated here was 18. Moreover, the potentially detrimental influence of fine particles on image segmentation even in media with larger average particle size should be evaluated on a case-specific basis.

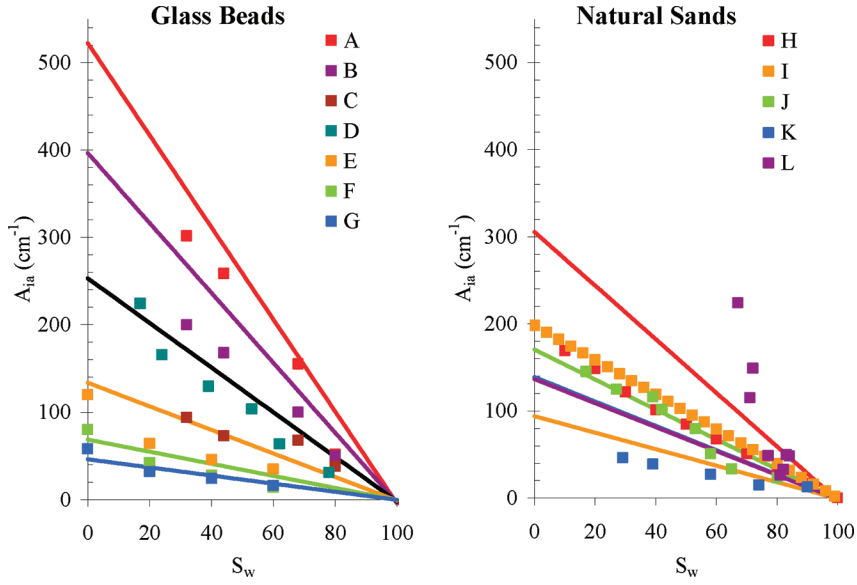


**FIGURE 6. Comparison of empirical model estimations (eq 1; lines) and literature air–water interfacial area ($A_{ia}$)–water saturation ($S_w$) relationships measured using a variety of aqueous-phase interfacial tracer methods (squares). The porous media for data sets C (brown) and D (teal) are the same; thus, a single model-estimation line (black) is shown for both. Data set I represents a reported empirical linear regression for a single medium, rather than discrete measurements. Estimations using eq 1 for data sets K (blue) and L (purple) overlap and are difficult to distinguish. Experimental data and porous media properties were obtained from A–C (*33*), D and J (*28*), E–G (*15*), H (*11*), I (*9*), K (*14*), and L (*21*).**

Data derived from $\mu$CT images were integrated across porous media to develop an empirical model for estimating total smooth interfacial area−water saturation relationships based solely on geometric surface area and porosity of the media. The model was found to provide reasonable estimates for a suite of model and natural sandy media for which experimental data were available, although estimated values were generally slightly higher than those measured experimentally using a variety of aqueous-phase interfacial tracers. Additional work is needed to clarify the cause of the higher estimations, including the role of image artifacts (i.e., voxelation), image processing methods (e.g., surface smoothing) and of interfacial accessibility constraints inherent to the experimental determinations. Additional porous media, including more complex natural media (e.g., high uniformity coefficient, more complex mineralogy, presence of fines) should be investigated to further evaluate the limits of the imaging methods and to refine the empirical model developed here.

The empirical model developed herein provides estimates of total smooth interfacial areas for use in describing solute fate and transport processes and in assessing the interfacial domains captured by indirect interfacial area measurement methods, such as interfacial tracer methods. The smoothed areas measured by $\mu$CT and represented by the empirical model are applicable to aqueous solute transport in variably saturated media. For example, dissolved interfacial tracers appear to be retained by the same interfacial domains as are measured by $\mu$CT. It is also likely that these same interfacial domains are responsible for the critical role the air–water interface plays in the retention of biotic and abiotic colloids (*3, 8, 34–36*). In contrast, gas-phase transport in porous media is known to be significantly influenced by interfacial micromorphology, which is not captured by $\mu$CT; thus, $\mu$CT-derived interfacial areas would be less relevant to gas-phase solute transport.

## Acknowledgments

We are grateful to the anonymous reviewers for their constructive comments. We are indebted to Mark Rivers (Advanced Photon Source) and Rick James, Benjamin Estabrook, and Tony Desautels (Middlebury College) for their assistance. This research was supported by grants provided by the U.S. Department of Agriculture National Research Initiative Program and by the Vermont EPSCoR Baccalaureate College Development Program, and by the support of Middlebury College. Microtomographic imaging was performed at GeoSoilEnviroCARS (Sector 13), Advanced Photon Source (APS), Argonne National Laboratory. GeoSoilEnviroCARS is supported by the National Science Foundation - Earth Sciences (EAR-0217473), Department of Energy - Geosciences (DE-FG02-94ER14466) and the State of Illinois. Use of the APS was supported by the U.S. Department of Energy, Office of Science, Office of Basic Energy Sciences, under Contract W-31-109-ENG-38.

## Supporting Information Available

Five additional figures are provided, including SEM images of the porous media, additional image processing results, and additional data extracted from the images. This material is available free of charge via the Internet at http://pubs.acs.org.

## Literature Cited

(1) Pennell, K. D.; Rhue, R. D.; Rao, P. S. C.; Johnston, C. T. Vapor-phase sorption of p-xylene and water on soils and clay minerals. *Environ. Sci. Technol.* **1992**, *26*, 756–763.

(2) Hoff, J. T.; Mackay, D.; Gillham, R. W.; Shlu, W. Y. Partitioning of organic chemicals at the air-water interface in environmental systems. *Environ. Sci. Technol.* **1993**, *27*, 2174–2180.

(3) Wan, J. M.; Wilson, J. L. Visualization of the role of the gas-water interface on the fate and transport of colloids in porous-media. *Water Resour. Res.* **1994**, *30*, 11–23.

(4) Valsaraj, K. T. Hydrophobic compounds in the environment: Adsorption equilibrium at the air-water interface. *Water Resour. Res.* **1994**, *28*, 819–830.

(5) Brusseau, M. L.; Popovicova, J.; Silva, J. A. K. Characterizing gas-water-interfacial and bulk-water partitioning for gas-phase transport of organic contaminants in unsaturated porous media. *Environ. Sci. Technol.* **1997**, *31*, 1645–1649.

(6) Schaefer, A.; Harms, H.; Zehnder, A. J. B. Bacterial accumulation at the air-water interface. *Environ. Sci. Technol.* **1998**, *32*, 3704–3712.

(7) Kim, H.; Annable, M. D.; Rao, P. S. C. Influence of air-water interfacial adsorption and gas-phase partitioning on the transport of organic chemicals in unsaturated porous media. *Environ. Sci. Technol.* **1998**, *32*, 1253–1259.

(8) Sirivithayapakorn, S.; Keller, A. Transport of colloids in unsaturated porous media: A pore-scale observation of processes during the dissolution of air-water interface. *Water Resour. Res.* **2003**, *39*, 1346–1355.

(9) Schaefer, C. E.; DiCarlo, D. A.; Blunt, M. J. Experimental measurement of air-water interfacial area during gravity drainage and secondary imbibition in porous media. *Water Resour. Res.* **2000**, *36*, 885–890.

(10) Chen, D.; Pyrak-Nolte, L. J.; Griffin, J.; Giordano, N. J. Measurement of interfacial area per volume for drainage and imbibition. *Water Resour. Res.* **2007**, *43*, W12504.

(11) Chen, L.; Kibbey, T. C. G. Measurement of air-water interfacial area for multiple hysteretic drainage curves in an unsaturated fine sand. *Langmuir* **2006**, *22*, 6874–6880.

(12) Hoeg, S.; Scholer, H. F.; Warnatz, J. Assessment of interfacial mass transfer in water-unsaturated soils during vapor extraction. *J. Contam. Hydrol.* **2004**, *74*, 163–195.

(13) Karkare, M. V.; Fort, T. Water movement in "unsaturated" porous media due to pore size and surface tension induced capillary pressure gradients. *Langmuir* **1993**, *9*, 2398–2403.

(14) Kim, H.; Rao, P. S. C.; Annable, M. D. Determination of effective air-water interfacial area in partially saturated porous media using surfactant adsorption. *Water Resour. Res.* **1997**, *33*, 2705–2711.

(15) Anwar, A.; Bettahar, M.; Matsubayashi, U. A method for determining air-water interfacial area in variably saturated porous media. *J. Contam. Hydrol.* **2000**, *43*, 129–146.

(16) Costanza-Robinson, M. S.; Brusseau, M. L. Air-water interfacial areas in unsaturated soils: Evaluation of interfacial domains. *Water Resour. Res.* **2002**, *38*, 1195–1211.

(17) Cheng, J.-T.; Pyrak-Nolte, L. J.; Nolte, D. D.; Giordano, N. J. Linking pressure and saturation through interfacial areas in porous media. *Geophys. Res. Lett.* **2004**, *31*, L08502.

(18) Costanza, M. S.; Brusseau, M. L. Contaminant vapor adsorption at the gas-water interface in soils. *Environ. Sci. Technol.* **2000**, *34*, 1–11.

(19) Bryant, S. L.; Johnson, A. Bulk and film contributions to fluid/fluid interfacial area in granular media. *Chem. Eng. Commun.* **2004**, *191*, 1660–1670.

(20) Brusseau, M. L.; Peng, S.; Schnaar, G.; Costanza-Robinson, M. S. Relationships among air-water interfacial area, capillary pressure, and water saturation for a sandy porous medium. *Water Resour. Res.* **2006**, *42*, W03501.

(21) Brusseau, M. L.; Peng, S.; Schnaar, G.; Murao, A. Measuring air-water interfacial areas with X-ray microtomography and interfacial partitioning tracer tests. *Environ. Sci. Technol.* **2007**, *41*, 1956–1961.

(22) Wildenschild, D.; Hopmans, J. W.; Vaz, C. M. P.; Rivers, M. L.; Rikard, D.; Christensen, B. S. B. Using X-ray computed tomography in hydrology: systems, resolutions, and limitations. *J. Hydrol.* **2002**, *267*, 285–297.

(23) Culligan, K. A.; Wildenschild, D.; Christensen, B. S. B.; Gray, W. G.; Tompson, A. F. B. Interfacial area measurements for unsaturated flow through a porous medium. *Water Resour. Res.* **2004**, *40*, W12413.

(24) Culligan, K. A.; Wildenschild, D.; Christensen, B. S. B.; Gray, W. G.; Rivers, M. L. Pore-scale characteristics of multiphase flow in porous media: A comparison of air-water and oil-water experiments. *Adv. Water Resour.* **2006**, *29*, 227–238.

(25) Rivers,M.L.http://cars9.uchicago.edu/software/idl/tomography.html, 2006.

(26) Ketcham, R. A. Computational methods for quantitative analysis of three-dimensional features in geological specimens. *Geosphere* **2005**, *1*, 32–41.

(27) Peng, S.; Brusseau, M. L. Impact of soil texture on air-water interfacial areas in unsaturated sandy porous media. *Water Resour. Res.* **2005**, *41*, W03021.

(28) Karkare, M. V.; Fort, T. Determination of the air-water interfacial area in wet "unsaturated" porous media. *Langmuir* **1996**, *12*, 2041–2044.

(29) Cary, J. W. Estimating the surface area of fluid phase interfaces in porous media. *J. Contam. Hydrol.* **1994**, *15*, 243–248.

(30) Or, D.; Tuller, M. Liquid retention and interfacial area in variably saturated porous media: Upscaling from single-pore to sample-scale model. *Water Resour. Res.* **1999**, *35*, 3591–3605.

(31) Kim, H.; Annable, M. D.; Rao, P. S. C. Gaseous transport of volatile organic chemicals in unsaturated porous media: effect of water-partitioning and air-water interfacial adsorption. *Environ. Sci. Technol.* **2001**, *35*, 4457–4462.

(32) Haughey, D.; Beveridge, G. Structural properties of packed beds: A review. *Can. J. Chem. Eng.* **1969**, *47*, 130–139.

(33) Silverstein, D. L.; Fort, T. Prediction of air-water interfacial area in wet unsaturated porous media. *Langmuir* **2000**, *16*, 829–834.

(34) Choi, H.; Corapcioglu, M. Y. Effect of colloids on volatile contaminant transport and air-water partitioning in unsaturated porous media. *Water Resour. Res.* **1997**, *33*, 2447–2457.

(35) Crist, J. T.; McCarthy, J. F.; Zevi, Y.; Baveye, P.; Throop, J. A.; Steenhuis, T. S. Pore-scale visualization of colloid transport and retention in partly saturated porous media. *Vadose Zone J.* **2004**, *3*, 444–450.

(36) Keller, A. A.; Sirivithayapakorn, S. Transport of colloids in unsaturated porous media: Explaining large-scale behavior based on pore-scale mechanisms. *Water Resour. Res.* **2004**, *40*, W12403.

ES072080D